Resonance Raman Investigation of Nickel Microperoxidase-11†

Jian-Guo Ma,‡ Jane M. Vanderkooi,§ Jun Zhang,‡ Song-Ling Jia,‡ and John A. Shelnutt*,‡

New Materials Theory and Validation Department, Sandia National Laboratories, Albuquerque, New Mexico 87185-1349, Department of Chemistry, The University of New Mexico, Albuquerque, New Mexico 87131, and Department of Biochemistry and Biophysics, University of Pennsylvania, Philadelphia, Pennsylvania 19104-6089

Received September 29, 1998; Revised Manuscript Received December 14, 1998

ABSTRACT: Resonance Raman and UV−visible absorption spectra show that nickel(II) microperoxidase-11 (NiMP-11) is four-coordinate in aqueous solution in the pH range from 1.0 to 13.0. In aqueous solutions of NiMP-11 in the absence of cetyltrimethylammonium bromide (CTAB), NiMP-11 is aggregated. In CTAB micellar solutions, where aggregation of NiMP-11 does not occur, the Raman spectra of NiMP-11 are similar to that of nickel(II) cytochrome *c* (NiCyt-*c*). The presence of the peptide segment shifts the equilibrium heavily in favor of the nonplanar form, just as does the entire protein component in the case of NiCyt-*c*. This further elucidates the structural mechanism by which the protein segment ruffles the heme, most likely modulating the redox potential as indicated for the cytochromes c_3 [Ma, J.-G., et al. (1998) *Biochemistry 37*, 12431−12442]. Furthermore, the hydrophobic environment that is provided by the CTAB micelle is found to be crucial to the native folding of the pentapeptide and formation of two hydrogen bonds in the peptide backbone. These two H-bonds act to contract the peptide segment exerting the force on the macrocycle that causes the ruffling and makes the redox potential more negative than if the heme were to remain planar. The structure of the heme and pentapeptide may also be associated with redox-linked triggering of the formation and release of cytochrome−protein complexes.

Nonplanar distortions of tetrapyrroles are prevalent in the hemes of hemoproteins, the pigments of photosynthetic proteins, and cofactor F_{430} of methylreductase (*1*). The nonplanarity of these porphyrin cofactors is currently believed to influence factors in the biological activity of the proteins, in part, because the heme deformations are often conserved within functional classes of proteins (*1*, *2*). It has been recognized for about 10 years that the hemes in many hemoproteins are highly distorted from planarity (*3*−*8*). Now, by using a new normal-coordinate structural decomposition procedure (*2*, *9*, *10*) for characterizing and quantifying heme distortions, our group has recently found that these distortions are often of different types for hemoproteins with different functions, but conserved for proteins belonging to the same functional class (*2*, *11*). Since nonplanar distortion is energetically unfavorable for heme (*12*), conservation of the heme conformation strongly suggests that physiological function might be modulated by protein control over the conformation of the heme prosthetic group.

The possible importance of nonplanar heme distortions is also emphasized by recent studies of model nonplanar porphyrins showing, first, that hemes are expected to be nearly planar in the absence of interactions with the protein moiety (*12*−*14*) and, second, that the nonplanar structure of the heme influences relevant chemical and photophysical properties (e.g., axial ligand affinity, redox potentials, transition dipoles and energies) (*4*, *7*, *10*, *15*−*17*). Moreover, the advent of many model nonplanar porphyrins has contributed to an improved understanding of the origin of nonplanar distortions of porphyrins. A great variety of sterically constrained nonplanar porphyrins have been synthesized, and their photophysical and chemical properties have been determined (*10*, *12*, *16*−*26*). These model studies indicate how the functional role of the porphyrin might be altered when the protein induces a particular distortion of the macrocycle.

One cannot take the point of view that the heme's function is solely to hold the iron atom in the protein with no further role in biological function in light of the conserved distortion of the heme. Instead, we take the usual view that conserved structural features in proteins should be examined as to their possible biochemical significance. We have previously shown that the conserved ruffling of the hemes of cytochromes c_3 most likely contributes to the tuning of the redox potentials (*14*). In a paper on Ni-reconstituted cytochrome *c*, we have shown that the ruffling is a consequence of the interaction of the heme with the protein, especially with the fingerprint pentapeptide (*27*) covalently linking the heme to the protein (*13*). The present paper further elucidates this structural mechanism, more clearly indicating the critical role of the pentapeptide and two H-bonds in this segment in causing the ruffling of the heme.

One of the major questions to be answered for heme proteins is how the protein moiety alters the structure of the bound heme group. In our previous report (*13*), the effect of pH-dependent changes in protein folding on the nonplanarity of the macrocycle in NiCyt-*c*[1] was studied by RR spectroscopy and MM calculations. NiCyt-*c* is a more appropriate

† Sandia is a multiprogram laboratory operated by Sandia Corp., a Lockheed Martin Co., for the United States Department of Energy under Contract DE-AC04-94AL85000.

* To whom correspondence should be addressed.

‡ Sandia National Laboratories and The University of New Mexico.

§ University of Pennsylvania.

10.1021/bi982332a CCC: $18.00
Published on Web 02/13/1999

model for the protein-induced changes in nonplanarity than the synthetic nonplanar porphyrins, and the interpretation of results from NiCyt-*c* is simplified by the lack of axial coordination at some pH values. The porphyrin of NiCyt-*c* is found to be nonplanar, and the nonplanarity decreases when the pH of the solution is lowered from 3 to 1 (*13*). The decreased nonplanarity was accounted for in terms of the disruption of a hydrogen-bonding network in the CAQCH segment upon lowering the pH. However, we could not conclusively show that this particular pentapeptide segment actually causes the heme distortion based on these NiCyt-*c* Raman results alone. MM calculations on MP-5 provide some evidence that the CAQCH segment alone can cause the macrocycle distortion, but Raman studies of a short peptide (NiMP-11) seemed to be a good way to limit the possible protein−heme interactions.

This work further focuses on the importance of the pentapeptide by showing that the heme distortion is increased by the peptide even when the rest of the protein and the Fe−histidine linkage are removed. Second, the pH-dependent behavior shows that the conformation of the fingerprint peptide, not just its presence, determines the heme structure. Third, the small distortion observed for the Ni-pentapeptide, which does not have the histidine bound to the metal, shows that the axial ligand bond is required to fully ruffle the heme. Fourth, and most important, the hydrophobic environment of the pentapeptide is crucial to the formation of the two hydrogen bonds in the peptide backbone and thus the near-native folding of the pentapeptide. These two H-bonds act to contract the peptide segment exerting the force on the macrocycle that causes the ruffling. One possible functional consequence of the resulting ruffling, based on model compound studies, is to make the redox potentials more negative than if the heme were planar. Other possible functional consequences associated with this structural mechanism are also discussed.

MATERIALS AND METHODS

Materials. NiMP-11 was prepared as follows: The iron-free porphyrin-MP-11 (pMP-11) was produced by treating 25 mg of microperoxidase (prepared by enzymatic degradation of equine heart cytochrome *c*, Sigma M-6756) with HF in an apparatus made of Teflon. Once approximately 2 mL of HF was transferred to the sample, aspiration was initiated to remove all HF. The pMP-11 was dissolved in a minimal volume of buffer [50 mM NH_4(OAc), pH ∼6.0]. The pMP-11 solution was then placed on a Sephadex G-50 column (2.5 × 100 cm) previously equilibrated with the buffer. The fractions of eluent absorbing at A_{620} were collected. The fractions were pooled, Ni(II) acetate was added to give a 10 mM solution (10 molar excess to the pMP-11), and the solution was adjusted to pH ∼3 with acetic acid. The solution was held at 75 °C in a bath for 4 h, with aliquots periodically removed to check by absorption changes for insertion of metal. The excess Ni(II) acetate was removed and the sample concentrated using Centricon concentrators from Amicon. These concentrators had a ∼3000 molecular weight cut off, and very little NiMP-11 passed the dialysis tubing. NiMP-11 samples in solutions at different pH values were used for obtaining spectra. NiMP-11 is stable in air and does not photodecompose. NiProtoP and NiMesoP were obtained from Porphyrin Products and used without further purification.

UV−Visible Absorption and Resonance Raman Spectroscopy. UV−visible absorption spectra were measured with an HP8452A (Hewlett-Packard) diode array spectrophotometer. Samples at different pH values were prepared before measurement and used as soon as possible. All spectra were taken at room temperature. The pH of the solution was measured with a Fisher Accumet Model 50 pH meter. The peak positions of the absorption bands were obtained by fitting the absorption spectra with Gaussian lines.

RR spectra were obtained using a partitioned Raman cell and a dual-channel spectrometer described previously (*28*). A Krypton ion laser (Coherent, INNOVA 20) provided the excitation wavelength (406.7 nm) in the Soret band region of the absorption spectrum. The scattered light was collected in the standard 90° scattering geometry. The solution samples were added to each side of a two-compartment Raman cell. The Raman cell was rotated at 50 Hz to prevent local heating of the sample and to probe alternately the sample and reference solutions.

All Raman spectra were taken at room temperature. Laser powers were 50 mW at the quartz cell. Sample integrity was monitored by examination of selected single scans of the Raman spectrum obtained during signal averaging and by UV−visible absorption spectra taken before and after exposure to laser light. No degradation of the sample was observed for all measurements. All spectra were corrected for nonlinearity of the spectrometer to obtain the absolute frequency positions of the lines (*13*). The peak positions of the Raman lines were obtained by fitting the Raman spectra with Lorentzian line shapes by using a nonlinear, least-squares curve-fitting program (Jandel Scientific) in which the peak frequency, peak intensity, line width, and a linear background were allowed to vary. The high-frequency component of the ν_{10} line (corresponding to the nearly planar conformer) is fitted using a Lorentzian line shape with line width fixed at 11 cm^{-1} (*13*). The low-frequency component of the ν_{10} line (corresponding to the nonplanar conformer) is also fitted using a Gaussian or Voigtian line shape. The trend in the intensity ratio holds regardless of which line shape is used in the curve fitting.

Molecular Mechanics Calculations. MM calculations were carried out using a modified version of POLYGRAF 3.21 software (Molecular Simulation, Inc.) and displayed on a Silicon Graphics workstation. The force constants were based on a normal coordinate analysis for NiOEP (*29*−*32*) and the DREIDING II force field (*33*). Equilibrium bond distances, angles, torsions, and inversions were adjusted to reproduce the crystal structure of the triclinic B form of NiOEP (*34*), using a force-field optimization routine. The force field for nickel porphyrins has been described in detail elsewhere (*16*) and has been adapted for other metals (*17*). Partial atomic charges used in determining the contribution of the electrostatic energy to the total energy were calculated using the charge equilibration method of Rappé and Goddard (*35*). Electrostatic charges were updated periodically during the

[1] Abbreviations: RR, resonance Raman; MM, molecular mechanics; NSD, normal-coordinate structural decomposition; MP, microperoxidase; MesoP, mesoporphyrin; ProtoP, protoporphyrin IX; Cyt-*c*, cytochrome *c*; CTAB, cetyltrimethylammonium bromide.

energy minimization. Recently, the accuracy of the calculations of porphyrin structures and conformational energies has been improved by using a modified version of the original force field (*25*). The main modification was the 50% reduction in the out-of-plane force constants to account for the fact that the in-plane and out-of-plane normal coordinate analyses were done independently. This version of the force field is used here, except that a dielectric constant of 79 was used to mimic the aqueous environment.

Normal-Coordinate Structural Decomposition. Jentzen and Shelnutt (*9*) have developed a method for classifying and quantifying the out-of-plane and in-plane distortions of the porphyrin macrocycle. In its simplest form, the NSD method uses a linear combination of only the six lowest-frequency out-of-plane normal coordinates of the macrocycle, one of each D_{4h} out-of-plane symmetry type, to simulate the macrocyclic distortion. In most cases, macrocyclic distortions can be described adequately by summing displacements along these six out-of-plane normal coordinates denoted *sad*, *ruf*, *dom*, *wav*(*x*), *wav*(*y*), and *pro*. Pure displacements along these coordinates are commonly observed symmetric deformations seen in X-ray crystal structures of symmetrically substituted porphyrins. The amounts of the saddling (*sad*), ruffling (*ruf*), doming (*dom*), waving [*wav*(*x*) and *wav*(*y*)], and propellering (*pro*) deformation types required to simulate the more complicated out-of-plane distortions of porphyrin macrocycle structures in proteins are determined by the NSD procedure. The NSD procedure has been successfully used to decompose and analyze the structures of all hemes of proteins in the Protein Data Bank (*2*) and many synthetic porphyrins (*25*). In this work, the energy-optimized structures were analyzed using the NSD method to quantify the out-of-plane distortions.

RESULTS AND DISCUSSION

Aggregation and Coordination State of NiMP-11 in Aqueous Solution. Absorption spectra of NiMesoP in different aqueous solutions are shown in Figure 1. The Soret band of NiMesoP at pH 13 is blue-shifted 18 nm compared to the Soret band of NiMesoP in aqueous CTAB micellar solution (Figure 1A,B). The Q-bands of the absorption spectrum of NiMesoP at pH 13 are red-shifted 4−6 nm when compared with the corresponding NiMesoP in CTAB solution. At pH 13, the Soret band is broader than that of NiMesoP in aqueous CTAB. The shifts and broadening are typical of aggregates of metalloporphyrins (*36*, *37*) and indicate the aggregation of NiMesoP in aqueous solution (*38*). In aqueous CTAB solution, NiMesoP is monomeric, showing no spectral changes in the pH range from pH 0.2 to 13 (see Figure 1B,C) (*39*). In addition, by comparison to the spectra of NiProtoP in micellar solution, a four-coordinate model (*13*, *40*), NiMesoP is also four-coordinate in aqueous CTAB in the pH range from 0.2 to 13.

The absorption spectra of NiMP-11 in the presence and absence of CTAB show similar shifts of the Soret and Q-bands as NiMesoP (shown in Figure 1D,E). The blue shift of the Soret band and red shifts of Q-bands indicate that, like NiMesoP, NiMP-11 is monomeric in aqueous CTAB but is aggregated in aqueous solution without detergent. By comparison of the spectrum of NiMP-11 in micellar solution to that of four-coordinate NiProtoP and NiMesoP, we find

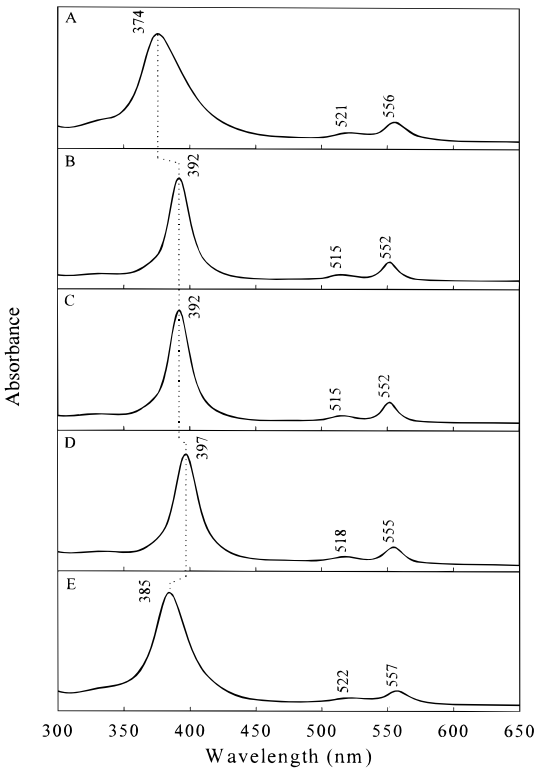

FIGURE 1: Optical absorption spectra of NiMesoP at pH 13.0 (A), in 9 mM CTAB at pH 13.0 (B) and pH 7.0 (C), of NiMP-11 in 9 mM CTAB at pH 7.0 (D), and of NiMP-11 at pH 7.0 (E).

that histidine is not bound to the nickel atom. For the axial-ligated species, the maximum of the Soret band would be at about 426 nm, and the intensity ratio of the β/α bands would be inverted (*13*). The absorption spectrum of NiMP-11 in CTAB solution is similar to that of four-coordinate NiCyt-*c* (*13*). Furthermore, no significant spectral changes are observed for NiMP-11 in CTAB solution in the pH range from pH 0.2 to 13 (*39*), indicating that NiMP-11 in aqueous CTAB is four-coordinate regardless of the pH.

The Peptide Segment of NiMP-11 Makes the Porphyrin Nonplanar. As shown in Figure 1C,D, the Soret and Q-bands of NiMP-11 are red-shifted 3−5 nm compared to the bands of NiMesoP. These red shifts are consistent with a more nonplanar porphyrin macrocycle (*16*, *17*, *20*). The nonplanarity of the porphyrin of NiMP-11 can also be detected by frequency shifts and band shape changes in the structure-sensitive Raman lines (*7*, *10*, *12*, *13*, *16*−*26*, *41*). The high (1300−1700 cm^{-1}) and low (150−550 cm^{-1}) frequency regions of the RR spectra of NiMesoP and NiMP-11 obtained in CTAB solution at pH 7.0 are shown in Figures 2 and 3, respectively. The frequencies of the structure-sensitive Raman lines ν_4, ν_3, ν_2, and ν_{10} for the CTAB solutions at different pH values are summarized in Table 1.

As can be seen from Figure 2, the structure-sensitive Raman lines ν_4, ν_3, and ν_2 of NiMP-11 are downshifted 1.3, 2.2, and 7.2 cm^{-1} (Table 1, pH 7.0) compared to the corresponding lines of NiMesoP. The downshifts of ν_4, ν_3, and ν_2 are consistent with a more nonplanar porphyrin (*10*, *13*, *16*, *17*, *23*) for NiMP-11. The frequency differences in the structure-sensitive Raman lines are negligible for different substituent groups (except for ν_2) in the absence of a change in macrocycle conformation, which is why they are good markers of porphyrin structure (*42*). Thus, shifts in the

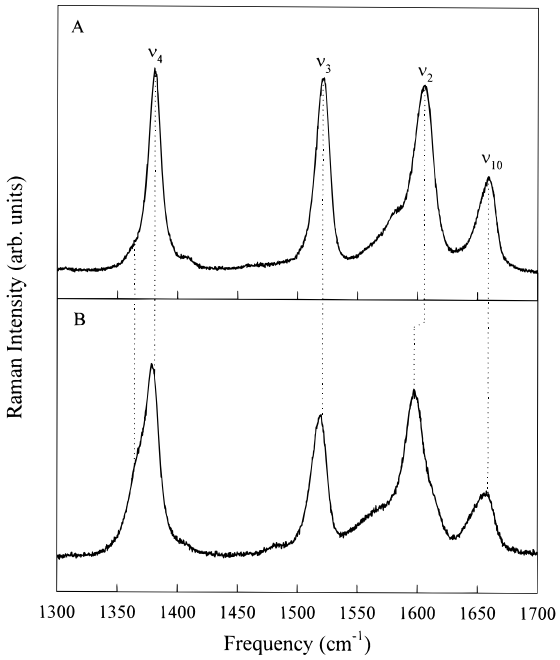

FIGURE 2: High-frequency region of resonance Raman spectra of NiMesoP in 9 mM CTAB at pH 7.0 (A) and of NiMP-11 in 9 mM CTAB at pH 7.0 (B).

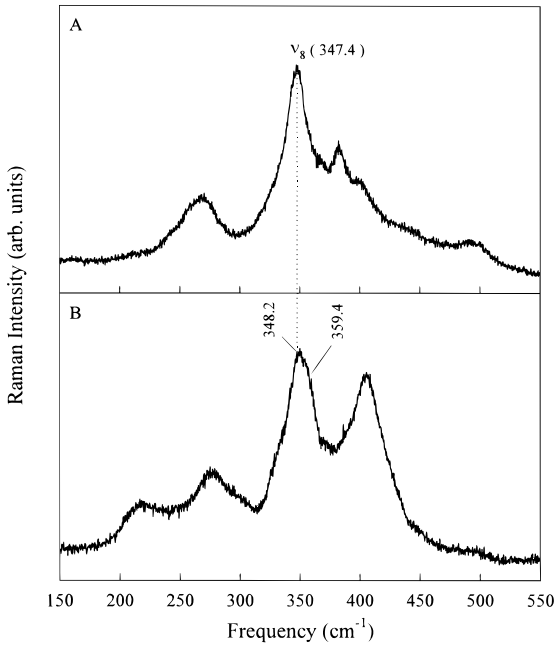

FIGURE 3: Low-frequency region of resonance Raman spectra of NiMesoP in 9 mM CTAB at pH 7.0 (A) and of NiMP-11 in 9 mM CTAB at pH 7.0 (B).

frequencies of the structure-sensitive Raman lines may be ascribed to differences in the porphyrin conformation. Specifically, ν_{10} of NiMP-11 is broader and more asymmetric than the line of NiMesoP. The Raman line ν_{10} is one of the most sensitive lines to nonplanar distortion of the porphyrin (*13*). The broadness and asymmetry indicate heterogeneity of the porphyrin structure (*7*, *12*−*14*). Anticipating the presence of multiple forms as the cause of the broadness of ν_{10}, we have resolved ν_{10} into two sublines. The high-frequency subline is associated with a nearly planar form based on its frequency (near 1660 cm^{-1}, see Table 1); the low-frequency subline (near 1650 cm^{-1}) is associated with a nonplanar form (*12*, *13*). The axially ligated species has ν_{10} at much lower frequency (1620 cm^{-1} or below), and does not interfere with the analysis of the data for the four-coordinate species (between 1660 and 1645 cm^{-1}). The frequencies of the two sublines of ν_{10} are lower for NiMP-11 than for NiMesoP at all pH values. In addition, the ratio of nonplanar-to-planar intensities of the sublines is larger for NiMP-11 than for NiMesoP. This shows that NiMP-11 has more of the nonplanar conformer than NiMesoP. This increase in the nonplanar conformer is attributed to the presence of the peptide segment attached to the porphyrin. Moreover, based on the lower frequency of the nonplanar subline, the nonplanar conformer of NiMP-11 is more nonplanar than that of NiMesoP.

Table 1: Frequencies (in cm^{-1}) of Structure-Sensitive Raman Lines of NiMesoP and NiMP-11 in Aqueous CTAB Micellar Solutions

pH	ν_4' [a]	ν_4	ν_3	ν_2	ν_{10}^{np}	ν_{10}^{p}	$\nu_{10}^{np}/\nu_{10}^{p}$ [b]
			NiMesoP				
1.0		1381.4	1522.4	1606.4	1653.3	1661.2	0.9
3.0		1381.1	1521.8	1606.1	1653.7	1661.2	0.8
7.0		1380.9	1521.0	1605.1	1652.8	1660.8	0.9
10.5		1380.7	1520.2	1604.5	1652.1	1660.2	1.0
13.0		1380.7	1520.2	1603.7	1651.7	1659.9	1.0
			NiMP-11				
1.0	1366.5	1380.0	1518.9	1599.4	1651.2	1659.8	3.4
3.0	1367.4	1379.8	1519.5	1599.1	1651.9	1660.1	2.4
7.0	1367.6	1379.6	1518.8	1597.9	1650.8	1659.9	1.9
10.5	1368.0	1379.6	1519.2	1598.1	1651.2	1660.1	1.9
13.0	1366.5	1379.4	1517.4	1597.4	1650.0	1659.5	3.7

[a] ν_4 line of the axially ligated minor species. [b] Ratio of areas of the nonplanar to planar sublines.

The low-frequency region (150−550 cm^{-1}) is consistent with the interpretation of the high-frequency spectrum. The macrocycle-breathing mode ν_8 is sensitive to macrocycle conformation (*25*), and as a rule, heterogeneity in the degree of out-of-plane distortion shows up in the shape of this line. In particular, the low-frequency components are associated with more planar conformers, and high-frequency sublines are associated with nonplanar conformers (*25*). From Figure 3, ν_8 of NiMP-11 (Figure 3B) is broad and asymmetric and can be resolved to two sublines. The ν_8 line of NiMesoP exhibits a narrow line at nearly the same place as the low-frequency component of ν_8 of NiMP-11. On this basis, one concludes that NiMP-11 has a more nonplanar porphyrin than NiMesoP, consistent with the interpretation of the Raman data in the high-frequency region (1300−1700 cm^{-1}). There are also other differences between NiMP-11 and NiMesoP in the low-frequency region of the spectra, e.g., differences in the lines near 216, 276, and 405 cm^{-1}. However, the interpretation of changes in these lines is ambiguous because of the lack of useful structural correlations.

While NiMP-11 is aggregated, the absorption spectrum does not indicate the same $\pi-\pi$ aggregation that occurs for NiMesoP. The difference in the type of aggregation for NiMP-11 and NiMesoP might give rise to the differences in ruffling. This is doubtful, however, because the monomeric form in CTAB is always more distorted than the aggregate in the absence of CTAB, which in turn is more ruffled than the model compound. Further, one might expect a pH-dependent change in aggregation and that this would be apparent in the Raman spectrum of NiMP-11 if aggregation causes an increase in ruffling. Instead, almost identical

Table 2: Out-of-Plane Displacements (Å) of the Minimal Basis Coordinates for the Energy-Minimized Structures of Fe(III) and Ni(II)MPs, Model Compounds, and the Horse Cytochrome *c* Crystal Structure[a]

structure	D_{oop}[b]	*ruf*	*sad*	*dom*	*wav(x)*	*wav(y)*	*pro*
cytochrome *c*[c]	1.049	1.004	−0.224	−0.020	0.122	0.161	−0.022
Fe(III)MP-11[d]	0.711	0.687	−0.150	0.086	−0.005	0.054	0.018
Fe(III)MP-11[e]	0.589	0.574	0.085	0.033	0.013	0.085	0.043
Fe(III)MP-8[d,f]	0.707	0.684	−0.150	0.085	−0.004	0.054	0.018
Fe(III)MP-8[e,f]	0.586	0.572	0.077	0.031	0.012	0.086	0.043
Fe(III)MP-8[d,g]	0.789	0.764	−0.173	0.074	0.029	0.035	0.024
Fe(III)MP-8[e,g]	0.579	0.563	0.098	0.025	0.020	0.073	0.050
Fe(III)MP-5[d]	0.786	0.762	−0.173	0.073	0.029	0.034	0.024
Fe(III)MP-5[e]	0.577	0.561	0.093	0.024	0.020	0.073	0.050
Fe(III)ProtoP-methyl sulfide[c,h]	0.136	−0.104	0.063	0.009	−0.043	0.011	0.041
Fe(III)MesoP	0.053	0.003	0.014	−0.015	−0.007	0.033	0.035
Fe(III)ProtoP[c]	0.068	0.002	0.036	−0.006	−0.025	0.052	0.000
Ni(II)MP-11	1.226	1.158	0.366	0.114	0.017	0.096	0.077
Ni(II)MP-5[c]	1.165	1.144	0.152	0.113	0.053	0.064	0.077
Ni(II)MesoPnp[i]	0.916	0.905	−0.128	−0.005	0.017	0.013	0.057
Ni(II)MesoPp[i]	0.065	0.006	0.022	−0.009	−0.005	0.044	0.041

[a] The initial structures used in the calculations were constructed from the X-ray crystal structure of horse heart ferricytochrome *c*. Fe(III)MPs are all axial-ligated. Ni(II)MPs are all four-coordinate. [b] Simulated total out-of-plane displacement. [c] Taken from ref 2. [d] The oxygens on propionates are fixed in the calculations. [e] The oxygens on propionates are not fixed in the calculations. [f] The amino acid sequence is -VQK***CAQCH***-. [g] The amino acid sequence is -***CAQCH***TVE-. [h] The vinyl groups of Fe(III)ProtoP were modified by two methylthioether groups. [i] np represents the nonplanar conformer; p represents the nearly planar conformer.

resonance Raman spectra are observed for NiMP-11 over the entire pH range from 1 to 13 (*39*).

From Figure 2B, a shoulder appears at the low-frequency side of the ν_4 line of the spectra of NiMP-11. The ν_4 line of NiMesoP has no such shoulder (Figure 2A). For NiMP-11, the shoulder is at about 1367 cm^{-1}, corresponding to an axially ligated species (*13*). The ν_3 and ν_2 lines of the axially ligated species, which would appear at about 1479 and 1577 cm^{-1}, are not present in the spectra because they are not as resonantly enhanced at this excitation wavelength as is ν_4. The shoulder of ν_4 indicates that there is a small amount of the axially ligated species for NiMP-11.

Molecular Mechanics Calculations of NiMP-11. MM calculations greatly aid in locating the forces in the protein moiety that control the nonplanar macrocyclic distortion. To evaluate the influence of the peptide segment on the porphyrin macrocycle of NiMP-11, we carried out MM calculations on NiMesoP, NiMP-5, and NiMP-11 with the histidine not bound to nickel to mimic the four-coordinate Ni porphyrins in aqueous solution. The amino acid sequence of NiMP-11 is -VQK***CAQCH***TVE-, including the fingerprint peptide segment -***CAQCH***-. All of the minimized structures are decomposed using the structural decomposition method to quantify the out-of-plane displacement of the porphyrin, and the decomposition results are listed in Table 2.

RR studies show that for NiMesoP in solution at least two conformers coexist differing in degree of nonplanarity. One of them is a nearly planar conformer; the other one is a nonplanar conformer. MM calculations, indeed, predict at least two such conformers and give an energy difference between these two conformers of only 0.5 kcal/mol. Thus, the calculations also predict an equilibrium mixture of these two conformers in solution. From Table 2, the total distortion of the nearly planar conformer of NiMesoP is only 0.065 Å, while the total distortion of the nonplanar conformer is 0.916 Å, and it is mainly ruffled with a secondary contribution from saddling. This is consistent with the analysis of the ν_{10} line of the RR spectra of NiMesoP in micellar solution.

When the fingerprint peptide segment is attached to the porphyrin, the total distortion increases to 1.165 Å (four-coordinate NiMP-5). The main type of deformation is also ruffling. No stable planar form is found in the MM calculations. Thus, the fingerprint peptide segment makes the porphyrin become more nonplanar. More amino acids added to the ends of the pentapeptide segment have little effect on the porphyrin conformation. The total distortion only increases by 0.061 Å (Table 2); i.e., the degree of nonplanarity of the porphyrin for NiMP-11 is almost the same as for NiMP-5.

The Fingerprint Peptide Segment Causes the Nonplanarity of the Heme for c*-Type Cytochromes.* In our previous studies on NiCyt-*c* and some model compounds (*13*), we show that the porphyrin of NiCyt-*c* is very nonplanar. Further, for four-coordinate NiCyt-*c*, the nonplanarity of the porphyrin changes with the pH. MM calculations show that the porphyrin becomes more nonplanar when the protein segment becomes more established and further that formation of the hydrogen bonds between the amide groups on the peptide backbone increases the nonplanarity (*13*). Although NiCyt-*c* does have a very nonplanar porphyrin, we could not conclusively demonstrate that a particular peptide segment (i.e., the fingerprint peptide) actually causes the heme distortion based on the NiCyt-*c* results alone. Now, NiMP-11, whose attached peptide includes the fingerprint segment, largely solves this problem. Indeed, the spectroscopic studies on NiMP-11 in aqueous micellar solution described above show that the porphyrin is very nonplanar, in fact close to distortion of NiCyt-*c*. In particular, the noted red shifts of the absorption bands and downshifts of the structure-sensitive Raman lines (Figures 1C,D, 2, and 3) of NiMP-11 are very close to those observed for NiCyt-*c*.

A Raman study by Desbois and co-workers (*43*) has shown that the nonplanar conformers observed in the X-ray structures of cytochromes *c* are probably also present in Fe(III)MP-8 in aqueous micellar solution. They conclude that the nonplanar conformation is essentially due to the three-point attachments between the heme and protein, i.e., the two thioether bridges and the Fe−His bond. Indeed, they showed that replacement of the proximal His with an exogenous His ligand results in a less distorted heme, based

on the shifts in the frequencies of two structure-sensitive Raman lines, ν_8 and ν_{10}. The use of these lines as markers of the nonplanarity of the iron porphyrin is based on the known behavior of these lines upon ruffling of nickel porphyrins (*7*, *10*, *41*, *44*).

To locate more specifically the forces that induce the heme distortion, we carried out MM calculations on several hypothetical Fe(III)MPs (MP-11, MP-8, and MP-5) and model compounds [ProtoP, MesoP, and ProtoP-di(methylthioether)] that vary in the size and other properties of the segment covalently attached to the macrocycle. The Fe(III)-MPs used in the calculations are constructed from the X-ray crystal structure of horse heart cytochrome *c* by removing all unrequired amino acids until the desired peptide segment was left. The peptide segment is bounded to the heme group via Cys14, Cys17, and His18 as in the crystal structure. The amino acid sequence of MP-11 is -VQK*CAQCH*TVE-. There are two kinds of MP-8 used in the calculations: one of them has the amino acid sequence as -VQK*CAQCH*-; the amino acid sequence of the other one is -*CAQCH*TVE-. For the Fe(III)MPs, the protein component was frozen in place at the crystal structure positions, and the hemes were allowed to relax in the protein environment during the minimization. The oxygens on the two propionates were fixed in place at the crystal structure positions to mimic the interactions of these groups with the rest of the protein (*14*). MM calculations were also carried out for all Fe(III)MPs with the propionate oxygens allowed to relax in the minimization. All of the minimized structures were analyzed by the normal-coordinate structural decomposition, and the results are listed in Table 2.

As can be seen from Table 2, Fe(III)ProtoP and Fe(III)-MesoP are both nearly planar; the total out-of-plane displacements are 0.068 and 0.053 Å, respectively. After thioether modifications of the vinyl substituents of Fe(III)ProtoP, the macrocycle becomes more distorted (D_{oop} = 0.136 Å) as a result of van der Waals interactions between the substituent groups. Ruffling is the major contributor (−0.104 Å) to the total distortion. Further, with the -***CAQCH***- pentapeptide segment attached, the total out-of-plane displacement increases greatly (D_{oop} = 0.786 Å). By comparison, the observed ruffling and total distortions for the horse heart cytochrome *c* crystal structure are only a little larger than those calculated for MP-5 (Table 2). Moreover, NSD results for Fe(III)MP-5, Fe(III)MP-8, and Fe(III)MP-11 show that the calculated structures are very close to each other (Figure 4), and to that of the X-ray structure of cytochrome *c*. These results together convincingly show that the fingerprint peptide segment is sufficient, in fact, to explain most of the normal-coordinate deformations making up the observed distortion of the heme of cytochrome *c* (*2*). Figure 4 shows that the three major contributors to the total distortions of the heme, saddling, ruffling, and waving [*wav(y)*], are all qualitatively predicted by the calculated structures of Fe(III)MPs.

We also addressed the question of the importance of the van der Waals interactions between the heme and the fingerprint peptide. We carried out two kinds of calculations: First, with the protein segment removed, we fixed the terminal carbons of the ethyl substituents of the heme in place at the crystal structure positions and let the heme relax in the minimization. This removes the van der Waals

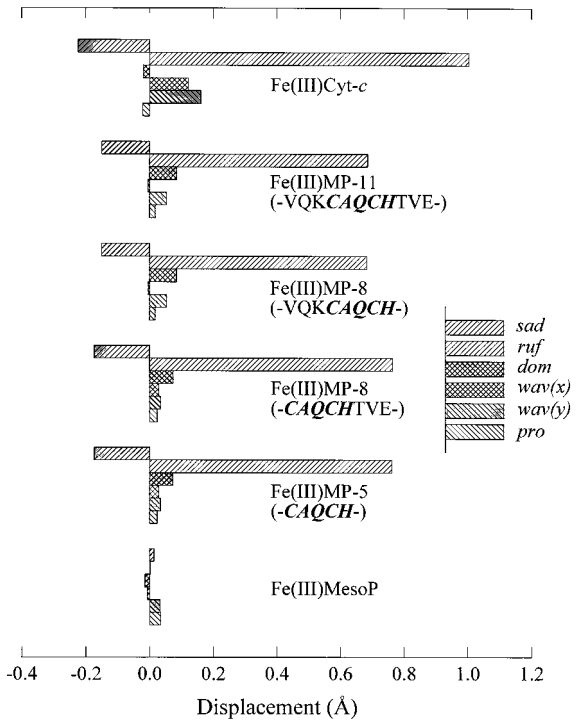

FIGURE 4: Out-of-plane displacements (minimal basis) for the heme group of the energy-optimized structures of Fe(III)MesoP, Fe(III)MP-5, Fe(III)MP-8 (-***CAQCH***TVE-), Fe(III)MP-8 (-VQK***CAQCH***-), Fe(III)MP-11, and the X-ray crystal structure of horse heart cytochrome *c*. The propionate oxygens are fixed in the calculated structures.

interactions, but holds the covalently linked heme substituents in the positions imposed by the peptide and the rest of the protein. Second, the terminal carbons and the propionate oxygens are both fixed in place at the crystal structure positions, and the heme is energy-minimized. The NSD results for the resulting structures show that the macrocycle is nearly planar (D_{oop} = 0.082 Å) with just the ethyl carbons fixed. Fixing the oxygens also increases the nonplanarity of the heme (D_{oop} = 0.210 Å). However, the total distortion is still much less than that of Fe(III)MP-5 or cytochrome *c*. These results further support a distortion mechanism based on the steric constraints imposed by the fingerprint peptide.

The rest of the protein also influences the distortion of the macrocycle. As an example, the negative saddling deformation of the heme in the crystal structure is not reproduced by the calculated Fe(III)MPs when the oxygens on the propionates are not fixed in the minimization (Table 2). Also, the total distortion is smaller for the MPs minimized with the oxygens released than for the MPs minimized with the oxygens fixed. Fixing the oxygens mimics the interactions between the heme propionates and the rest of the protein, mainly hydrogen bonding between the heme propionates and the protein. This interaction may account for the saddling deformation of the heme of cytochrome *c*, consistent with a similar conclusion obtained from MM calculations on the hemes in cytochromes c_3 (*14*).

Finally, we should point out the differences expected for nickel and the native Fe(III) heme. First, as shown previously by computational methods (*13*), the absence of histidine coordination to the metal results in less distortion. Breaking the Fe−His bond essentially makes one of the two H-bonds in the backbone less effective in exerting a buckling force

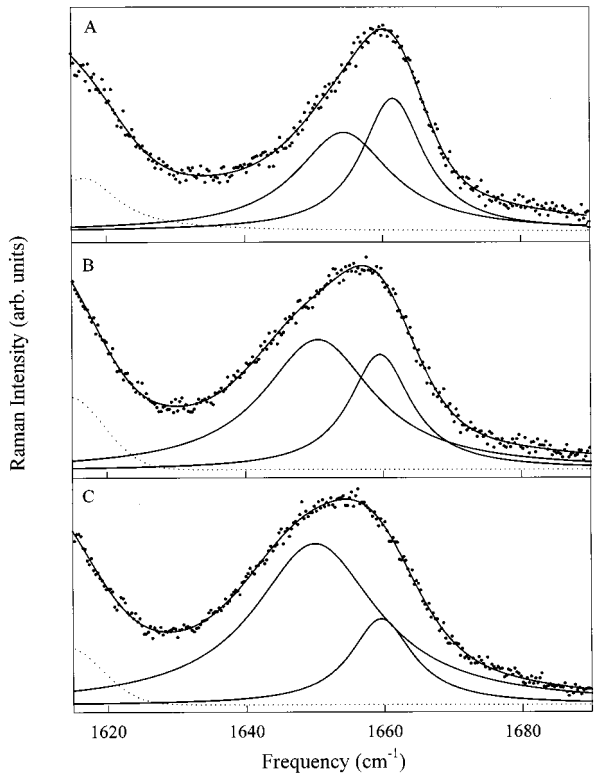

FIGURE 5: Lorentzian decomposition of the ν_{10} resonance Raman lines in the spectra of NiMP-11 in aqueous solution at pH 7.0 (A) and in 9 mM CTAB micellar solution at pH 7.0 (B) and pH 13.0 (C). The line width of the high-frequency component of ν_{10} was fixed at 11 cm^{-1}. All other line parameters were allowed to vary in the curve fit (*13*).

on the macrocycle. In opposition to this effect of Ni substitution, low-spin Ni(II) prefers shorter metal−nitrogen bonds to the pyrroles than Fe(III), and this favors more ruffling for nickel. Apparently, the loss of the axial ligand has the larger effect since the planar form of NiMP-11 is present to some extent under all solution conditions.

Effects of the Hydrophobic Lipid Environment of the Heme Peptide on Porphyrin Distortion. Figure 5 shows the Lorentzian decomposition of the ν_{10} RR line of NiMP-11 in aqueous solution at pH 7.0 (Figure 5A) and in CTAB micellar solutions at pH 7.0 (Figure 5B) and 13.0 (Figure 5C). The ratio of nonplanar-to-planar intensities, as measured by the areas of the sublines of ν_{10} for NiMP-11, is 1.1 in aqueous solution at pH 7.0. The frequency of the nonplanar subline is at 1654.4 cm^{-1}. The spectra of NiMP-11 at other investigated pH values (pH 1, 3, 10.5, and 13) in the absence of detergent are almost identical (*39*). The spectrum of NiMP-11 in the CTAB micelles shows that the porphyrin is more nonplanar (compare Figures 5B and 5A), based on the downshift of the nonplanar subline (to 1650.8 cm^{-1}) and the increased ratio (1.9) of the nonplanar-to-planar intensities of ν_{10} of NiMP-11 in CTAB solutions (Table 1). The changes in the nonplanarity of the porphyrin are probably not caused by the lack of aggregation of NiMP-11 in CTAB since NiMesoP, with and without CTAB, does not show these spectral differences (*39*). Thus, the hydrophobic micellar environment of the peptide segment is apparently required to shift the equilibrium strongly in favor of the nonplanar form. Because of the similarity of the spectra of NiMP-11 in CTAB and Ni cytochrome *c*, we conclude that the protein component of cytochrome *c* must provide a similar hydrophobic environment for the fingerprint peptide.

Another interesting feature in the Raman spectra is that the relative area of the subline corresponding to the nonplanar form is much greater for NiMP-11 in CTAB solution at pH 1.0 and 13.0 than at the other investigated pH values (Table 1). This can also be seen by comparing the spectra shown in Figure 5B,C. In addition, the line shape ν_{10} at pH 1.0 is similar to that at pH 13.0, but line shapes of ν_{10} at pH 3.0 and 10.5 are similar to that at pH 7.0. Thus, the heme when in CTAB becomes more nonplanar at the pH extremes (pH 1 and 13) than for a broad pH range about neutral pH. In contrast, for NiMP-11 in aqueous solution in the absence of CTAB, the relative areas of the nonplanar and nearly planar sublines hardly change at all in the pH range from 1.0 to 13.0. Thus, the hydrophobic environment is essential for the peptide segment to induce the nonplanar distortion of the porphyrin at pH extremes.

The pH dependence for the micellar solutions of NiMP-11 may be understood in terms of the relative solvent exposure of the peptide. Referring to the pK_a values of the amino acids of the peptide segment, one finds that the N-terminus and the side chain of Lys13 are positively charged when the pH of the solution is below about 3. At pH values that are above 10.5, the C-terminus and the side chain of Glu21 are negatively charged. The peptide segment has the largest number of charges near neutral pH where both termini and the side chains of Glu21 and Lys13 are all charged. [The protonation and/or deprotonation of the termini and side chains are estimated based on the pK_R of the free amino acids (*45*) and the values obtained by Marques, Munro, and co-workers (*46*, *47*). The possible influences of the propionates are excluded since NiMesoP does not show these spectral changes; i.e., the relative intensities of the nearly planar and nonplanar sublines do not change with pH (Table 1).] The charged groups would prefer a location near the surface of the micelle to the hydrophobic interior of the micelle, regardless of the sign of the charge. The decrease in number of charges at the pH extremes increases the hydrophobicity of one end or the other of the peptide, allowing the -CAQC- segment to be more surrounded by the hydrophobic environment of the micelle. This environment favors the formation of strong hydrogen bonds in the fingerprint peptide backbone, possibly including the same two H-bonds observed in the X-ray crystal structure of cytochrome *c* (*2*, *13*). These two hydrogen bonds compress the peptide segment exerting a buckling force on the macrocycle and making the porphyrin become more nonplanar (*13*). This interpretation suggests that the protein that surrounds the fingerprint peptide provides a similar hydrophobic environment that allows the hydrogen bonds to form in cytochrome *c*.

One functional consequence of this structural mechanism, based on model-compound studies (*4*), is to make the redox potentials more negative than if the heme were planar. One must be aware, however, that many other factors besides ruffling also influence redox potentials. This structural mechanism may also be associated with triggering the formation and release of protein−cytochrome *c* complexes. In particular, the complex with cytochrome *c* peroxidase binds to cytochrome *c* at the site of the fingerprint pentapeptide, which is very near the surface. Thus, a redox-linked

conformational change in the heme structure would be directly coupled to the protein−protein interface through an induced conformational change in the pentapeptide. Furthermore, binding of the reaction partner at this site would change the hydrophobicity at the pentapeptide, altering the strength of the H-bonds and the conformation of the pentapeptide, thus modifying the heme conformation and consequently its redox properties.

These important new heme structural issues need to be further addressed with regard to the function of *c*-type cytochromes. Moreover, the structural mechanisms by which the protein moiety of cytochrome *c* causes the conserved heme distortion need to be fully understood for comparisons with other proteins. The heme distortion mechanism for cytochrome *c* can then be contrasted with noncovalent structural mechanisms that must be operative in causing heme distortions in other proteins that lack covalent linkages. Large conserved heme distortions, such as the 1-Å saddling of the heme in peroxidases and the 0.8-Å ruffling in nitrophorins, must be caused by other yet unknown means (*48*).

SUMMARY AND CONCLUSIONS

NiMP-11 is four-coordinate in aqueous solution in the pH range from 1.0 to 13.0. In aqueous solutions in the absence of detergent (CTAB), NiMP-11 is aggregated. In CTAB micellar solutions, where aggregation of NiMP-11 is not a problem, the Raman spectra of NiMP-11 are similar to those of NiCyt-*c*. The presence of the peptide segment shifts the equilibrium strongly in favor of the nonplanar form, just as does the entire protein component in the case of NiCyt-*c*. MM calculations on the heme−peptide and model compounds (*49*) show that the fingerprint peptide segment is the major cause of the nonplanar distortion of the porphyrin. More amino acids added to the ends of the fingerprint peptide segment have little effect on the porphyrin conformation. These calculations strongly support a distortion mechanism in which the nonplanar distortion of the heme in cytochrome *c* is caused by interactions with the fingerprint peptide segment. Furthermore, the porphyrin of NiMP-11 is more nonplanar in the micellar CTAB solution than in aqueous solution without detergent. The hydrophobic environment provided by the micelle is essential in causing the nonplanarity of the porphyrin for NiMP-11. Moreover, the Raman results show that the nonplanarity of NiMP-11 in CTAB solution is greatest at pH extremes of 13.0 and 1.0. Similarly, the hydrophobicity of the peptide segment is greater at these pH extremes than at neutral pH. This suggests that the increase in the hydrophobicity of the environment surrounding the fingerprint peptide favors the formation of the hydrogen bonds, which are observed in the backbone of the fingerprint peptide in the crystal structure of cytochrome *c*. These hydrogen bonds exert forces on the macrocycle that make the porphyrin nonplanar. In the absence of detergent micelles, the H-bonds are weaker because of the less hydrophobic environment and cause less distortion. The proven influence of macrocycle distortions on redox potentials has obvious biological consequences for electron-transport proteins such as cytochrome *c*. An associated structural mechanism for triggering redox-linked formation and release of protein−protein complexes is suggested.

REFERENCES

1. Shelnutt, J. A., Song, X.-Z., Ma, J.-G., Jia, S.-L., Jentzen, W., and Medforth, C. J. (1998) *Chem. Soc. Rev. 27*, 31−41.
2. Jentzen, W., Ma, J.-G., and Shelnutt, J. A. (1998) *Biophys. J. 74*, 753−763.
3. Geno, M. K., and Halpern, J. (1987) *J. Am. Chem. Soc. 109*, 1238−1240.
4. Barkigia, K. M., Chantranupong, L., Smith, K. M., and Fajer, J. (1988) *J. Am. Chem. Soc. 110*, 7566−7567.
5. Furenlid, L. R., Renner, M. W., Smith, K. M., and Fajer, J. (1990) *J. Am. Chem. Soc. 112*, 1634−1635.
6. Furenlid, L. R., Renner, M. W., Smith, K. M., and Fajer, J. (1990) *J. Am. Chem. Soc. 112*, 8987−8989.
7. Alden, R. G., Ondrias, M. R., and Shelnutt, J. A. (1990) *J. Am. Chem. Soc. 112*, 691−697.
8. Tetreau, C., Lavalette, D., Momenteau, M., Fischer, J., and Weiss, R. (1994) *J. Am. Chem. Soc. 116*, 11840−11848.
9. Jentzen, W., Song, X.-Z., and Shelnutt, J. A. (1997) *J. Phys. Chem. B 101*, 1684−1699.
10. Jentzen, W., Simpson, M. C., Hobbs, J. D., Song, X., Ema, T., Nelson, N. Y., Medforth, C. J., Smith, K. M., Veyrat, M., Mazzanti, M., Ramasseul, R., Marchon, J.-C., Takeuchi, T., Goddard, W. A., III, and Shelnutt, J. A. (1995) *J. Am. Chem. Soc. 117*, 11085−11097.
11. Hobbs, J. D., and Shelnutt, J. A. (1995) *J. Protein Chem. 14*, 19−25.
12. Anderson, K. K., Hobbs, J. D., Luo, L., Stanley, K. D., Quirke, J. M. E., and Shelnutt, J. A. (1993) *J. Am. Chem. Soc. 115*, 12346−12352.
13. Ma, J.-G., Laberge, M., Song, X.-Z., Jentzen, W., Jia, S.-L., Zhang, J., Vanderkooi, J. M., and Shelnutt, J. A. (1998) *Biochemistry 37*, 5118−5128.
14. Ma, J.-G., Zhang, J., Franco, R., Jia, S.-L., Moura, I., Moura, J. J. G., Kroneck, P. M. H., and Shelnutt, J. A. (1998) *Biochemistry 37*, 12431−12442.
15. Shelnutt, J. A. (1989) *J. Phys. Chem. 93*, 6283−6290.
16. Shelnutt, J. A., Medforth, C. J., Berber, M. D., Barkigia, K. M., and Smith, K. M. (1991) *J. Am. Chem. Soc. 113*, 4077−4087.
17. Sparks, L. D., Medforth, C. J., Park, M.-S., Chamberlain, J. R., Ondrias, M. R., Sengo, M. O., Smith, K. M., and Shelnutt, J. A. (1993) *J. Am. Chem. Soc. 115*, 581−592.
18. Medforth, C. J., and Smith, K. M. (1990) *Tetrahedron Lett. 31*, 5583−5586.
19. Shelnutt, J. A., Majumder, S. A., Sparks, L. D., Hobbs, J. D., Medforth, C. J., Senge, M. O., Smith, K. M., Miura, M., Luo L., and Quirke, J. M. E. (1992) *J. Raman Spectrosc. 23*, 523−529.
20. Medforth, C. J., Senge, M. O., Smith, K. M., Sparks, L. D., and Shelnutt, J. A. (1992) *J. Am. Chem. Soc. 114*, 9859−9869.
21. Sparks, L. D., Scheidt, W. R., and Shelnutt, J. A. (1992) *Inorg. Chem. 31*, 2191−2196.
22. Sparks, L. D., Chamberlain, J. R., Hsu, P., Ondrias, M. R., Swanson, B. A., Oritiz de Montellano, P. R., and Shelnutt, J. A. (1993) *Inorg. Chem. 32*, 3153−3163.
23. Hobbs, J. D., Majumder, S. A., Luo, L., Sickelsmith, G. A., Quirke, J. M. E., Medforth, C. J., Smith, K. M., and Shelnutt, J. A. (1994) *J. Am. Chem. Soc. 116*, 3261−3270.
24. Medforth, C. J., Senge, M. O., Forsyth, T. P., Hobbs, J. D., Shelnutt, J. A., and Smith, K. M. (1994) *Inorg. Chem. 33*, 3865−3872.
25. Song, X.-Z., Jentzen, W., Jia, S.-L., Jaquinod, L., Nurco, D. J., Medforth, C. J., Smith, K. M., and Shelnutt, J. A. (1996) *J. Am. Chem. Soc. 118*, 12975−12988.
26. Jia, S.-L., Jentzen, W., Shang, M., Song, X.-Z., Ma, J.-G., Scheidt, W. R., and Shelnutt, J. A. (1998) *Inorg. Chem. 37*, 4402−4412.
27. Martinez, S. E., Huang, D., Szczepaniak, A., Cramer, W. A., and Smith, J. L. (1994) *Structure 2*, 95−105.
28. Shelnutt, J. A. (1983) *J. Phys. Chem. 87*, 605−616.

29. Abe, M., Kitagawa, T., and Kyogoku, Y. (1978) *J. Chem. Phys. 69*, 4526−4534.
30. Li, X.-Y., Czernuszewics, R. S., Kincaid, J. R., and Spiro, T. G. (1989) *J. Am. Chem. Soc. 111*, 7012−7023.
31. Li, X.-Y., Czernuszewics, R. S., Kincaid, J. R., Stein, P., and Spiro, T. G. (1990) *J. Phys. Chem. 94*, 47−61.
32. Li, X.-Y., Czernuszewics, R. S., Kincaid, J. R., Su, Y. O., and Spiro, T. G. (1990) *J. Phys. Chem. 94*, 31−47.
33. Mayo, S. L., Olafson, B. D., and Goddard, W. A., III (1990) *J. Phys. Chem. 94*, 8897−8909.
34. Brennan, T. D., Scheidt, W. R., and Shelnutt J. A. (1988) *J. Am. Chem. Soc. 110*, 3919−3924.
35. Rappé, A. K., and Goddard, W. A., III (1991) *J. Phys. Chem. 95*, 3358−3363.
36. Gust, D., Moore, A. L., Luttrull, D. K., DeGraziano, J. M., Bodt, N. J., Auweraer, M. V., and De Schryver, F. C. (1991) *Langmuir 7*, 1483−1490.
37. Luk, S. Y., Mayers, R., Williams, J. O. (1988) *Thin Solid Films 157*, 69−79.
38. Song, X., Miura, M., Xu, X., Taylor, K. K., Majumder, S. A., Hobbs, J. D., Cesarano, J., and Shelnutt, J. A. (1996) *Langmuir 12*, 2019−2027.
39. Ma, J.-G., and Shelnutt, J. A., unpublished experimental results.
40. Shelnutt, J. A., Alston, K., Ho, J.-Y., Yu, N.-T., Yamamoto, T., and Rifkind, J. M. (1986) *Biochemistry 25*, 620−627.
41. Alden, R. G., Crawford, B. A., Doolen, R., Ondrias, M. R., and Shelnutt, J. A. (1989) *J. Am. Chem. Soc. 111*, 2070−2072.
42. Spiro, T. G. (1983) in *Iron Porphyrins*, *Part Two* (Lever, A. B. P., and Gray, H. B., Eds.) Chapter 3, Addison-Wesley Publishing Company, Reading, MA.
43. Othman, S., Lirzin, A. L., and Desbois, A. (1994) *Biochemistry 33*, 15437−15448.
44. Czernuszewicz, R. S., Li, X.-Y., and Spiro, T. G. (1989) *J. Am. Chem. Soc. 111*, 7024−7031.
45. Lehninger, A. L. (1978) in *Biochemistry*, Chapter 4, p 79, Worth Publishers, Inc., New York.
46. Marques, H. M., Shongwe, M. S., Munro, O. Q., and Egan, T. J. (1997) *S. Afr. J. Chem. 50*, 166−180.
47. Munro, O. Q., and Marques, H. M. (1996) *Inorg. Chem. 35*, 3752−3767.
48. Howes, B. D., Schiødt, C. B., Welinder, K. G., Marzocchi, M. P., Ma, J.-G., Zhang, J., Shelnutt, J. A., and Smulevich, G. (1999) *Biophys. J.*, submitted for publication.
49. Shelnutt, J. A. (1999) in *Handbook of Porphyrins and Related Macrocycles: Biomaterials for Materials Scientists, Chemists, and Physicists* (Kadish, K. M., Smith, K. M., and Guilard, R., Eds.) Academic Press, New York (in press).

BI982332A